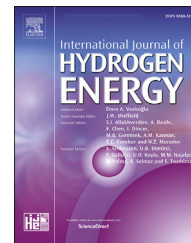


Available online at www.sciencedirect.com

ScienceDirect

journal homepage: www.elsevier.com/locate/ijhydene

Oxygen reduction reaction and hydrogen evolution reaction catalyzed by carbon-supported molybdenum-coated palladium nanocubes

Wei Yan^a, Wen Wu^a, Kai Wang^a, Zhenghua Tang^{a,b,*},
Shaowei Chen^{a,c,**}

^a Guangzhou Key Laboratory for Surface Chemistry of Energy Materials, New Energy Research Institute, School of Environment and Energy, South China University of Technology, Guangzhou Higher Education Mega Centre, Guangzhou, 510006, China

^b Guangdong Provincial Key Laboratory of Atmospheric Environment and Pollution Control, Guangdong Provincial Engineering and Technology Research Center for Environmental Risk Prevention and Emergency Disposal, School of Environment and Energy, South China University of Technology, Guangzhou Higher Education Mega Centre, Guangzhou, 510006, China

^c Department of Chemistry and Biochemistry, University of California, 1156 High Street, Santa Cruz, CA 95064, United States

ARTICLE INFO

Article history:

Received 7 February 2018

Received in revised form

29 June 2018

Accepted 15 July 2018

Available online 4 August 2018

Keywords:

Palladium nano-

cubes@molybdenum

Core-shell structure

Dual electrocatalytic functionalities

Oxygen reduction reaction

Hydrogen evolution reaction

ABSTRACT

Oxygen reduction reaction (ORR) and hydrogen evolution reaction (HER) are two important processes for electrochemical energy storage and conversion. Herein, we describe the preparation of carbon-supported Pd nanocubes@Mo core@shell nanostructures as efficient dual catalysts for both ORR and HER. The core@shell structure was manifested by high-resolution transmission electron microscopy measurements, including high angle-angular dark field-scanning transmission electron microscopy and elemental mapping analysis. Further structural insights were obtained in X-ray diffraction and X-ray photoelectron spectroscopy measurements. The nanostructures exhibited apparent electrocatalytic activity toward both ORR and HER, and the performances were markedly higher than those without the deposition of a Mo overlayer. In ORR, the activity was even better than that of commercial Pt/C within the context of onset potential, specific and mass activities; whereas in HER, the performance of Pd nanocubes@Mo core@shell nanostructures remained subpar as compared to that of Pt/C in terms of the overpotential to reach the current density of 10 mA cm⁻², the Tafel slope was comparable and the stability was excellent. The excellent electrocatalytic performance can be attributed to the Pd-Mo synergistic effects imparted from the core-shell structure.

© 2018 Hydrogen Energy Publications LLC. Published by Elsevier Ltd. All rights reserved.

* Corresponding author. Guangzhou Key Laboratory for Surface Chemistry of Energy Materials, New Energy Research Institute, School of Environment and Energy, South China University of Technology, Guangzhou Higher Education Mega Centre, Guangzhou, 510006, China.

** Corresponding author. Guangzhou Key Laboratory for Surface Chemistry of Energy Materials, New Energy Research Institute, School of Environment and Energy, South China University of Technology, Guangzhou Higher Education Mega Centre, Guangzhou, 510006, China.

E-mail addresses: zhht@scut.edu.cn (Z. Tang), shaowei@ucsc.edu (S. Chen).

<https://doi.org/10.1016/j.ijhydene.2018.07.097>

0360-3199/© 2018 Hydrogen Energy Publications LLC. Published by Elsevier Ltd. All rights reserved.

Introduction

Oxygen reduction reaction (ORR) and hydrogen evolution reaction (HER) are two important processes in the development of sustainable and green energy technologies for electrochemical energy conversion and storage [1–4]. Because of their complicated reaction pathways and sluggish electron-transfer kinetics, development of low-cost, high-performance catalysts is needed. Currently, Pt-based materials are the state-of-art catalysts for both ORR and HER [5–7]. However, the low natural abundance and high costs of Pt have significantly hindered the widespread commercialization of such technologies. In addition, Pt-based electrocatalysts typically exhibit insufficient long-term durability during the electrocatalytic operations, mainly due to Ostwald ripening and deactivation by adsorption of CO-like poisonous intermediates on the catalyst surface [8–10]. Therefore, substantial research efforts have been devoted to the design and development of non-Pt catalysts for both ORR and HER [11–15].

In fact, palladium has been recognized as a viable alternative, mainly due to its relatively low cost, desirable electrocatalytic performance and well-established techniques toward industrial applications [16–18]. For instance, the abundance of Pd in the Earth's crust is 0.015 ppm by weight, which is 3 times higher than that of Pt (0.005 ppm) [19]. Advanced Pd-based catalysts have been widely employed in the electrocatalysis of ORR and HER. For instance, Huang et al. developed a simple process based on controlled pyrolysis for the synthesis of palladium-cobalt nanoparticles supported on carbon nanotubes and observed apparent ORR and HER activity [20]. In another study, Liu and co-workers reported the preparation of porous Pd nanoparticle assemblies, which exhibited a small Tafel slope of 30 mV s^{-1} , and an exceptional low overpotential (η_{100}) of 80 mV to reach the current density of 100 mA cm^{-2} for HER in 0.5 M H_2SO_4 , as well as a half-wave potential of 0.837 V and an onset potential of 0.926 V at 1600 rpm with a scan rate of 5 mV s^{-1} for ORR in 0.1 M KOH [21].

The catalytic activity of Pd may be further enhanced by a range of structural engineering [22–25], such as surface modification [26], manipulation of composition and morphology [27,28], and alloying with transition metals [29]. For instance, in a recent study [30], Lee and Kwon deposited Pd nanoparticles (ca. 7 nm) on MoS_2 surfaces by a one-step sonochemical method and observed enhanced electrocatalytic activity towards ORR in alkaline media. This was ascribed to the tensile strain produced at the Pd/ MoS_2 interface and the charge-transfer from Pd to MoS_2 that raised the Pd d-band center. Note that a range of molybdenum-based compounds, such as MoS_2 [31], MoO_3 [32], Mo_2C [33], and MoNi_4 [34], are also active in HER electrocatalysis. Thus, it will be of fundamental and technological significance to examine the dual activity of the resulting composites towards both ORR and HER. This is the primary motivation of the present study.

In this study, we report a facile approach to the preparation of carbon-supported palladium nanocubes that were decorated with a thin layer of molybdenum compounds as dual functional electrocatalysts for both ORR and HER.

Transmission electron microscopic measurements and elemental mapping analysis showed the formation of well-defined Pd nanocubes@Mo core-shell structures. In electrochemical tests, the nanostructures demonstrated superior activity and markedly higher long-term stability than Pt/C for ORR. In addition, in HER tests, the sample also displayed a remarkable performance that was comparable to that of Pt/C, with exceedingly enhanced durability. This was largely ascribed to the lattice strain at the Pd/Mo interface that manipulated the electronic interactions with reaction intermediates hence enhanced the catalytic activity.

Materials and methods

Chemicals

Poly(vinyl pyrrolidone) (PVP, MW = 55,000), L-ascorbic acid (99%), potassium bromide (KBr, 99%), sodium tetrachloropalladate(II) (Na_2PdCl_4 , 99.95%), acetic acid glacial (99.5%), ammonium molybdate ($(\text{NH}_4)_6\text{Mo}_7\text{O}_{24}\cdot 4\text{H}_2\text{O}$, 99%), and carbon black (Vulcan XC-72, Cabot) were purchased from Energy Chemicals. All aqueous solutions were prepared using de-ionized (DI) water with a resistivity of $18.3 \text{ M}\Omega \text{ cm}$.

Synthesis of Pd nanocubes

Pd nanocubes were synthesized by adopting a literature protocol [35]. In a typical procedure, 8 mL of an aqueous solution containing PVP (105 mg), ascorbic acid (60 mg), and KBr (600 mg) was heated at 80°C under magnetic stirring at 800 rpm for 10 min. Then 3 mL of an aqueous solution containing 0.2 mmol Na_2PdCl_4 was added quickly. The mixture was heated at 80°C in air under magnetic stirring for 3 h and then cooled down to room temperature. Pd nanocubes were collected by centrifugation and washed three times with a water/acetone mixture to remove excess PVP.

Preparation of Pd nanocubes@Mo core@frame nanostructure

For the synthesis of Mo-coated Pd nanocubes [35], in a typical process, 2 mg of $(\text{NH}_4)_6\text{Mo}_7\text{O}_{24}\cdot 4\text{H}_2\text{O}$ and 12 mg of ascorbic acid were added into 10 mL of the aqueous suspension of Pd nanocubes obtained above (1 mg mL^{-1}). After heating at 80°C under magnetic stirring for 2 h, the reaction solution was cooled down to room temperature, affording Pd nanocubes@Mo core@frame nanostructures that were collected by centrifugation and washed three times with water.

Preparation of carbon-supported Pd nanocubes and Pd nanocubes@Mo nanostructures

To prepare carbon-supported Pd nanocubes (denoted as Pd nanocubes/C), Pd nanocubes were collected by centrifugation and re-dispersed in 10 mL of ethanol. A specific amount of carbon black (Vulcan XC-72, Cabot) was added into the suspension, and the loading of Pd was controlled at 20 wt %. The mixture was then stirred and sonicated for 6 h. The resultant Pd nanocubes/C composites were collected by centrifugation.

Residual PVP and bromide on the composite surface were removed by re-dispersing the sample in 10 mL of acetic acid, and heated at 60 °C for 2 h under magnetic stirring. The preparation of carbon supported Pd nanocubes@Mo core@frame nanostructures (denoted as Pd nanocubes@Mo/C) was carried out in the same manner.

Characterizations

The morphology of the samples was examined with a high-resolution transmission electron microscope (JEOL TEM-2010). SEM images were collected with a field-emission scanning electron microscope (FESEM, Merlin). X-ray diffraction (XRD) patterns were acquired on a Bruker D8 diffractometer with a Cu K α radiation ($\lambda = 0.1541$ nm). The surface chemical composition and valence state of the samples were studied by X-ray photoelectron spectroscopy (XPS) measurements with a VG MultiLab 2000 instrument with a monochromatic Al K α X-ray source (Thermo VG Scientific).

In a typical ORR test, 2 mg of the catalyst prepared above was dispersed in 1 mL of anhydrous ethanol, and 10 μ L of 5 wt % Nafion was added into the mixture and sonicated for about 30 min. Then, 10 μ L of the mixture was dropcast onto the glassy carbon electrode of a rotating ring-disk electrode and dried at room temperature. The catalyst loadings were all 102 μ g cm $^{-2}$ (The geometrical area of rotating disk electrode is 0.196 cm $^{-2}$). Cyclic voltammetric (CV) measurements were conducted at the potential scan rate of 10 mV s $^{-1}$, and linear sweep voltammograms (LSV) were collected in an O $_2$ -saturated 0.1 M KOH solution at the scan rate of 10 mV s $^{-1}$ with the rotation rates varied from 225 to 2025 rpm. Chronoamperometric measurements were conducted in an O $_2$ -saturated 0.1 M KOH solution at +0.5 V for 38,000 s. Accelerated durability tests (ADT) of the catalysts were conducted with the potential cycled in an O $_2$ -saturated 0.1 M KOH solution between +0.6 and +1.0 V at the scan rate of 50 mV s $^{-1}$. The electrochemically active surface areas (ECSA) of the catalysts were estimated in a N $_2$ -saturated 0.1 M HClO $_4$ solution at room temperature at the scan rate of 50 mV s $^{-1}$.

In a HER test, 5 mg of the catalysts prepared above and 50 μ L of 5 wt % Nafion was dispersed in 1 mL of ethanol. Then, 10 μ L of the mixture was dropcast onto a glassy carbon electrode and dried at room temperature. LSV was collected in 0.5 M H $_2$ SO $_4$ solution at the scan rate of 10 mV s $^{-1}$.

Results and discussions

Schematic illustration of the preparation of Pd nanocube@Mo nanostructures

The preparation of the Pd nanocubes and molybdenum coated Pd nanocubes is schematically depicted in Scheme 1. Pd nanocubes were first synthesized by thermal reduction of Pd $^{2+}$ in the presence of PVP, KBr, and ascorbic acid (AA) at 80 °C, which then reacted with Mo $^{6+}$ for 2 h to generate Mo-coated Pd nanocubes [35]. The obtained samples were then loaded onto carbon surface by mixing with a calculated amount of carbon black. Note that, KBr is used as the capping agent and surfactant to avoid the aggregation. And it plays the

role for facet selection by surface passivation [36,37]. The detailed procedure is included in the experimental section.

TEM analysis of carbon-supported Pd nanocubes and Pd nanocubes@Mo

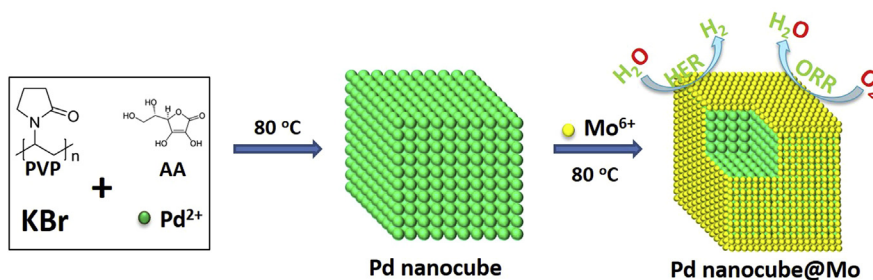
The morphologies and surface microstructures of the carbon-supported Pd nanocubes and Pd nanocubes@Mo samples were first studied by TEM measurements. Fig. 1a and b shows the representative TEM images of the Pd nanocubes/C sample, where a number of dark contrast objects (Pd nanotubes) were distributed onto a low-contrast matrix (carbon). The Pd particles exhibited a well-defined cubic shape with an edge length of approximately 10 nm, and an interplanar spacing of 0.195 nm (Fig. 1b) that is consistent with that of the Pd (200) planes [38]. Upon the coating of a Mo layer, such a well-defined cube morphology was preserved, as manifested in Fig. 2b and d. Interestingly, the crystalline lattice spacing in the core was found to diminish somewhat to 0.185 nm (Fig. 1d), suggesting that upon the coating of Mo slight shrinkage of the Pd crystal lattices occurred [39,40].

The coating of a Mo layer on Pd nanocubes was evidenced in elemental analysis. Fig. 1e and f shows two orthogonal line scans of a single Pd nanocubes@Mo particle. In both scan profiles, the Pd concentration was markedly higher than that of Mo, and Mo was slightly enriched at the edges, consistent with the formation of a thin Mo layer on the Pd nanocube surface. Such a structure is also manifested in high-angular dark-field scanning transmission electron microscopic (HAADF-STEM) measurements. From the elemental maps in Fig. 1g–j, one can see that Pd was evenly decorated with a Mo overlayer.

XRD and XPS studies of Pd nanocubes/C and Pd nanocubes@Mo/C

Further structural insights were obtained in X-ray diffraction (XRD) and X-ray photoelectron spectroscopy (XPS) measurements. As depicted in Fig. 2a, both Pd nanocubes/C and Pd nanocubes@Mo/C samples exhibited four well-defined diffraction peaks. For Pd nanocubes/C, these can be easily identified at $2\theta = 40.1^\circ$, 46.7° , 68.1° , and 82.1° , consistent with the (111), (200), (220), (311) diffractions of fcc Pd (JCPDS card# 46-1043). Yet, upon the coating of Mo on the Pd nanocube surface, the 2θ values of the diffraction peaks can be found to increase slightly, suggesting a decrease of the lattice spacing in Pd nanocubes@Mo nanostructures (no Mo diffraction features were observed, likely because of its low concentration, vide infra). This observation is in good accordance with results obtained in TEM studies (Fig. 1e).

Fig. 2b and c shows the high-resolution XPS spectra of Pd 3d electrons in Pd nanocubes/C and Pd nanocubes@Mo/C, respectively. In both samples, deconvolution yields two doublets. The doublets at the binding energy of 335.5 eV and 340.8 eV can be assigned to metallic Pd(0), while the peaks at somewhat higher binding energies of 337.1 eV and 342.4 eV to Pd(II) [22,23,41,42]. Furthermore, based on the integrated peak areas, the Pd(0)-to-Pd(II) ratio can be calculated to be 1.16 and 0.80 for Pd nanocubes/C and Pd nanocubes@Mo/C, respectively, suggesting that upon the coating of a Mo overlayer on



Scheme 1 – Schematic illustration of the preparation of Pd nanocube@Mo structures.

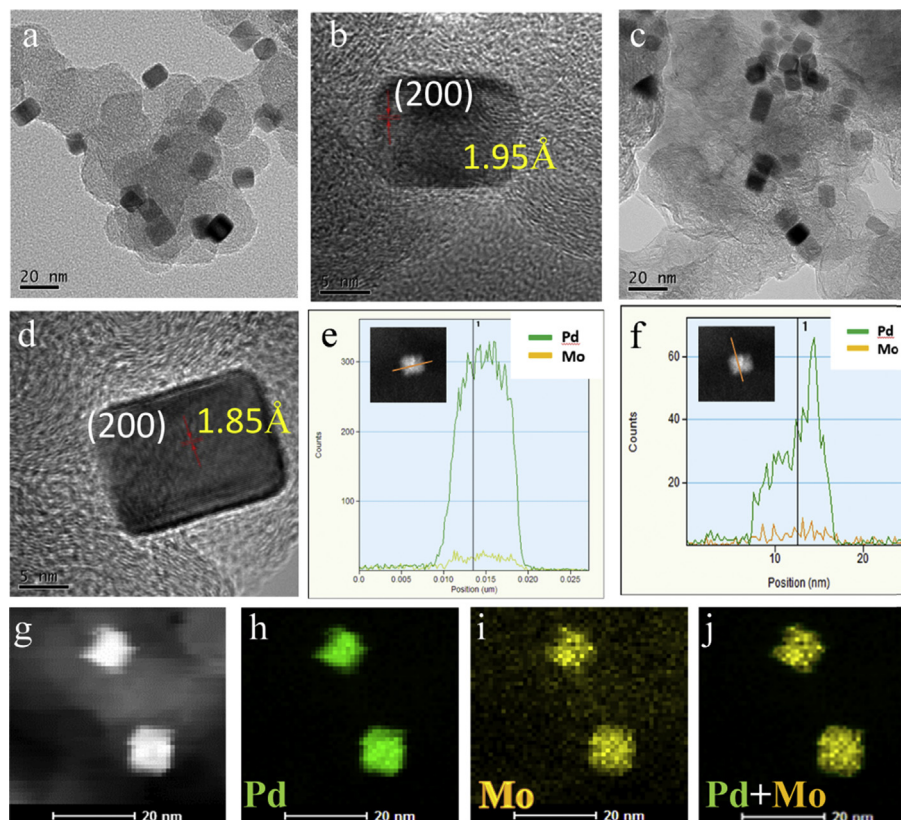


Fig. 1 – Representative TEM images of (a, b) Pd nanocubes/C and (c, d) Pd nanocubes@Mo/C. Panels (e) and (f) are the corresponding line scan profiles of Pd nanocubes@Mo in two orthogonal directions (red lines in the respective inset). Typical HAADF-STEM image of (g) Pd nanocubes@Mo/C and the corresponding elemental maps of (h) Pd, (i) Mo, and (j) Pd + Mo. (For interpretation of the references to color in this figure legend, the reader is referred to the Web version of this article.)

Pd nanocube surfaces, electron transfer likely occurred from Pd to surface Mo. In addition, the high resolution XPS spectra of Mo 3d electrons is depicted in Fig. 2d. Upon de-convolution, three pairs of doublets with binding energies at 235.4 eV and 232.3 eV, 233.7 eV and 231.4 eV, 230.1 eV and 227.8 eV can be easily identified, which are ascribed to Mo^{6+} , Mo^{4+} , and Mo^0 , respectively [34,43,44]. As a note, based on the XPS survey scan results, the Pd-to-Mo atomic ratio can be estimated as 1: 0.09.

Electrocatalytic ORR activities of Pd nanocubes/C and Pd nanocubes@Mo/C

The electrocatalytic activity toward ORR was then tested for the two samples and compared with commercial Pt/C. As

shown in Figure S1, in O_2 -saturated 0.1 M KOH, Pd nanocubes/C, Pd nanocubes@Mo/C, and Pt/C all exhibited a sharp cathodic peak around +0.7 V ~ +0.8 V, in contrast to the featureless response when the solution was saturated with N_2 , suggesting apparent ORR activity. Fig. 3a shows the rotating ring-disk electrode (RRDE) measurements of the samples, where one can see that as the electrode potential was swept negatively, nonzero current started to emerge. Yet the onset potential (E_{onset}) varied among the samples, +0.92 V for Pd nanocubes/C, +0.97 V for Pd nanocubes@Mo/C, and +0.96 V for Pt/C. A consistent variation was observed with the half-wave potential ($E_{1/2}$), +0.80 V for Pd nanocubes/C, +0.84 V for Pd nanocubes@Mo/C, and +0.81 V for Pt/C. These results suggest that the coating of a Mo overlayer on Pd nanocubes

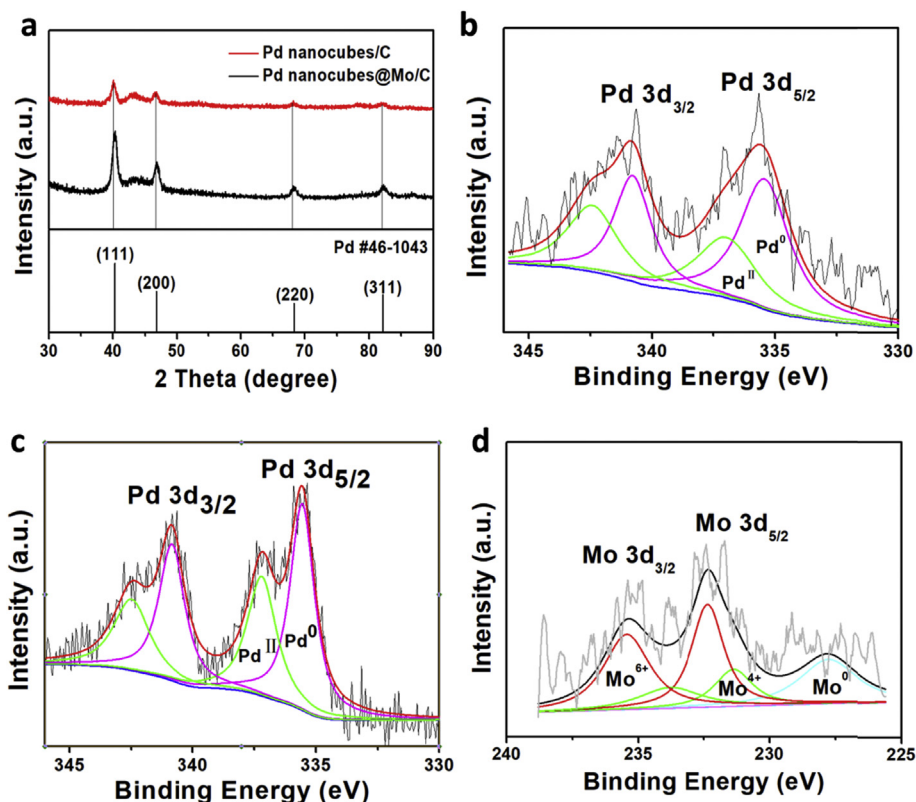


Fig. 2 – (a) XRD patterns of Pd nanocubes/C and Pd nanocubes@Mo/C; (b, c) High-resolution XPS spectra of Pd 3d electrons for Pd nanocubes/C and Pd nanocubes@Mo/C; (d) High-resolution XPS spectra of Mo 3d electrons for Pd nanocubes@Mo/C.

markedly enhanced the ORR activity, with a performance even superior to that of commercial Pt/C. In fact, the diffusion-limited current density of Pd nanocubes@Mo was even greater than that of Pt/C.

Furthermore, one can see that the disk currents were approximately 20 times higher than those at the ring electrode, suggesting the production of only a minimal amount of peroxide intermediates. In fact, the number of electron transfer (n) and H_2O_2 yield in the ORR process can be calculated by equations (1) and (2)

$$n = \frac{4I_d}{I_d + I_r/N} \quad (1)$$

$$\text{H}_2\text{O}_2\% = \frac{200I_r/N}{\frac{I_r}{N} + I_d} \quad (2)$$

where I_d is the disk current, I_r is the ring current, and N is the collection efficiency of RRDE (0.37). From Fig. 3b, one can see that the calculated n values in the range of 0 V to +0.8 V were almost invariant at 3.81 to 3.99 for the three samples. This suggests that ORR proceeds with a highly efficient, direct 4-electron transfer pathway. Correspondingly, the H_2O_2 yield was found to be below 10%, indicating that the production of peroxide intermediates was negligible.

Further analysis of the catalytic performance was carried out with RRDE measurements at varied rotation rates (Figure S2). It can be seen that the ORR currents all increased with increasing electrode rotation rate. The corresponding Koutecky-Levich (K-L) plots were depicted in Figure S3, where

all three samples exhibited linear profiles with rather consistent slopes within the potential range of +0.06 V to +0.21 V. This suggests that ORR proceeded with a first-order kinetics with regard to the oxygen concentration dissolved in the solution [22,23,45].

The reaction kinetics and associated mechanistic insight can be further analyzed and compared from the Tafel plots. As shown in Fig. 3c, the Tafel plots include two clear regions at high and low overpotentials, which has been well documented in previous reports [9,13,45,46]. In the low overpotential range, the Tafel slope was determined to be 55.4 mV dec^{-1} , 57.9 mV dec^{-1} , and 64.6 mV dec^{-1} for Pd nanocubes/C, Pd nanocubes@Mo/C, and Pt/C, respectively, all close to 60 mV dec^{-1} , suggesting the rate determining step in the ORR process was probably a pseudo two-electron reaction [22,23]. In the high overpotential range, the slope was 107.9 mV dec^{-1} , 111.7 mV dec^{-1} , and 115.9 mV dec^{-1} for Pd nanocubes/C, Pd nanocubes@Mo/C, and Pt/C, respectively, indicating that the reaction rate was predominantly governed by the first electron transfer to the oxygen molecules [13,46].

In addition, based on the electrochemically active surface area (ECSA, Figure S4), the ECSA value can be determined by equation (3) [41,47]:

$$\text{ECSA} = \frac{Q_H}{m \times q_H} \quad (3)$$

where Q_H is the charge for H_{upd} adsorption, m is the metal loading mass, and q_H is the charge required for monolayer adsorption of hydrogen on a Pd surface (405 $\mu\text{C}/\text{cm}^2$). The

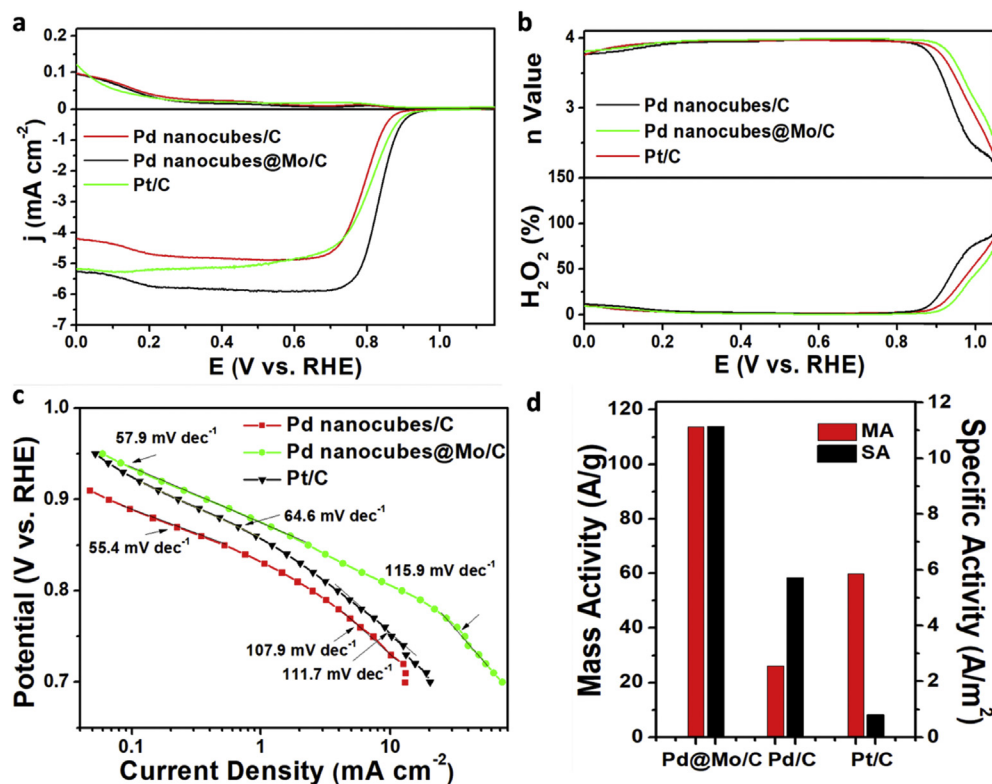


Fig. 3 – (a) LSV curves of Pd nanocubes/C, Pd nanocubes@Mo/C, and Pt/C in an O₂-saturated 0.1 M KOH solution at a sweep rate of 10 mV s⁻¹ and electrode rotation of 1600 rpm. Ring potential was set at +1.5 V. (b) Numbers of electron transfer and the corresponding H₂O₂ yields, (c) Tafel plots and (d) comparison of specific activity and mass activity at 0.85 V of Pd nanocubes/C, Pd nanocubes@Mo/C, and Pt/C.

specific activity (SA) and mass activity (MA) of the samples were determined and compared in Fig. 3d. It can be seen that at 0.85 V, Pd nanocubes@Mo/C exhibited a SA value of 11.13 A/m², approximately twice that of Pd nanocube/C and 13 times higher than that of Pt/C for Pt. The Pd nanocubes@Mo/C sample also possessed a high MA value of 113.76 A/g_{Pd}, about 4 times that of Pd nanocubes/C and 2 times that of Pt/C. These results strongly attest the significant impact of a Mo overlayer on the ORR activity of Pd nanocubes. Note that, such intriguing ORR performance can be probably attributed to the synergistic effects between the Pd core and the Mo overlayer, as manifested by the electron transfer behaviors observed in XPS measurements. For bimetallic core-shell structures, previous investigations have shown that the lattice mismatch at the boundary of the core and the surrounded shell would create lattice strain over several atomic layers at the interface, which is probably favourable for accelerating the kinetics of the electrocatalytic process [48–52].

Long-term durability of Pd nanocubes/C, Pd nanocubes@Mo/C, and commercial Pt/C for ORR

The stability for long-term operation was then compared. Fig. 4a shows the chronoamperometric responses at 0.5 V. It can be seen that even after continuous operation for 11 h, the current retained 90.6% of its initial value for the Pd nanocubes@Mo/C, much higher than that of Pd nanocubes/C

(84.5%) and Pt/C (78.1%). Consistent results were obtained in accelerated durability tests (ADT), in which polarization curves were recorded before and after the catalysts were subject to 5000 cycles of potential scans in the potential range of +0.4 V to +1.2 V at 50 mV s⁻¹ in an O₂-saturated 0.1 M KOH. As depicted in Fig. 4b–d, after 5000 cycles of potential scans, E_{1/2} shifted negatively by only 7 mV for Pd nanocubes@Mo/C, markedly lower than that of Pd nanocubes/C (10 mV) and Pt/C (15.7 mV). This further attests the remarkable long-term stability of Pd nanocubes@Mo/C, as compared to the Pd nanocubes/C and Pt/C catalysts.

Electrocatalytic performance of Pd nanocubes/C, Pd nanocubes@Mo/C and Pt/C towards HER

The electrocatalytic performance towards HER was also evaluated and compared among the series of samples. Electrochemical measurements were carried out in 0.5 M H₂SO₄ at a scan rate of 10 mV s⁻¹ by linear sweep voltammetry. As illustrated in Fig. 5a, Pt/C exhibited a nearly zero onset potential, whereas for Pd nanocubes/C and Pd nanocubes@Mo/C, the onset potentials were some more negative, at -0.09 and -0.02 V, respectively. In addition, to reach the current density of 20 mA cm⁻², the overpotential was 206 mV, 97 mV and 11 mV for Pd nanocubes/C, Pd nanocubes@Mo/C and Pt/C, respectively. These suggest that the coating of a Mo overlayer significantly enhanced the HER activity of Pd nanocubes

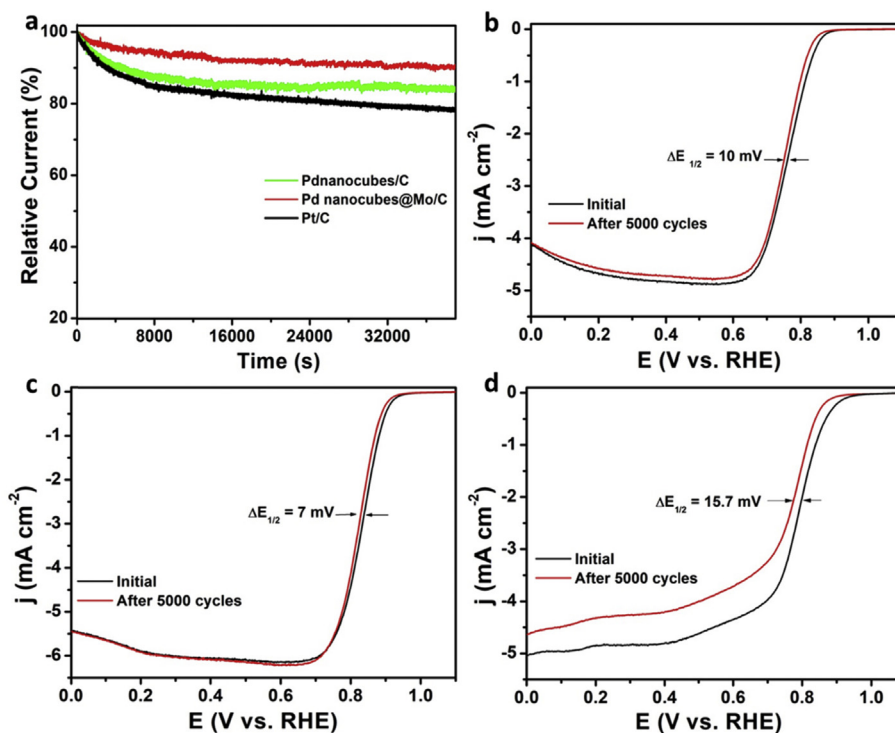


Fig. 4 – Chronoamperometric responses for ORR at Pd nanocubes/C, Pd nanocubes@Mo/C, and commercial Pt/C electrodes in an O₂-saturated 0.1 M KOH solution for 38,000 s at 0.5 V (a). The accelerated durability tests (ADT) of Pd nanocubes/C (b) and Pd nanocubes@Mo/C (c) and commercial Pt/C (d) were carried out by before and after 5000 cycles between 0.6 and 1.0 V at a scan rate of 50 mV s⁻¹ with a rotation speed of 1600 rpm in an O₂-saturated 0.1 M KOH solution.

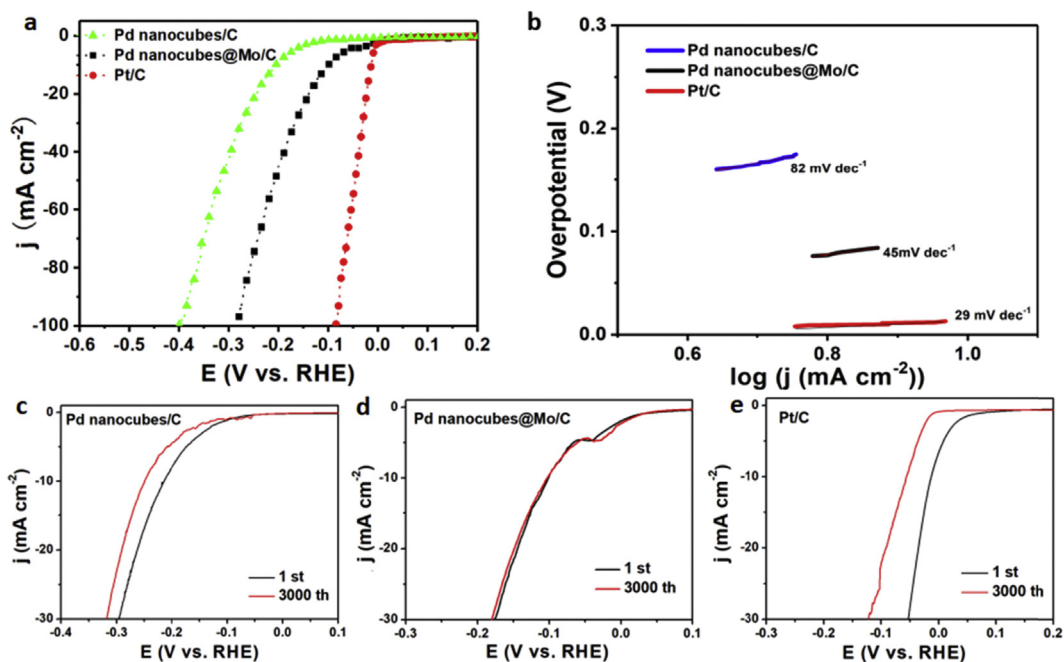


Fig. 5 – (a) Linear sweep voltammograms (LSV) of Pd nanocubes/C, Pd nanocubes@Mo/C, and Pt/C in 0.5 M H₂SO₄. (b) The Tafel plots for Pd nanocubes/C, Pd nanocubes@Mo/C, and Pt/C in 0.5 M H₂SO₄. (c–e) LSV curves of Pd nanocubes/C, Pd nanocubes@Mo/C, and Pt/C in 0.5 M H₂SO₄ before and after cycling tests.

towards HER, although the performance remained subpar as compared to that of Pt/C.

To evaluate the HER reaction kinetics, Tafel slope was quantitatively estimated by linear regression of the polarization curves according to the Tafel equation, $\eta = b \log j + a$ (j is the current density and b is the Tafel slope). From Fig. 5b, the Tafel slope for Pt/C was estimated to be 29 mV dec⁻¹, in good consistence with results reported previously [53,54]; and it was markedly higher at 82 mV dec⁻¹ and 45 mV dec⁻¹ for Pd nanocubes/C and Pd nanocubes@Mo/C, respectively, indicating that the HER process was probably governed by the Volmer-Heyrovsky mechanism. Note that according to this mechanism, the reaction rate is determined by electrochemical desorption of hydrogen from the catalyst surface [55–57].

Note that, the ORR activity of Pd nanocubes@Mo/C is superior than recently reported PdMo based similar materials. The comparison results are compiled in Table S1. For instance, the onset potential and diffusion-limited current density at +0.45 V were 0.96 V and 4.64 mA cm⁻², 0.80 V and 3.40 mA cm⁻², 0.90 V and 3.70 mA cm⁻², 0.93 V and 3.85 mA cm⁻², for Pd nanoparticles on Mo₂C nanotubes (Mo₂C-Pd-9%) [58], carbon supported Pd₉₀Mo₁₀ nanoparticles (Pd₉₀Mo₁₀-900 °C) [59], three dimensional palladium nanoparticles on reduced graphene oxide (3D-Pd/rGO) [60], and Pd nanoparticle assemblies (Pd NPs) [21], both values are lower than that of Pd nanocubes@Mo/C (0.97 V and 5.88 mA cm⁻²) in this work. In addition, the HER activity is also close to that of the above materials (Table S1).

Catalytic durability represents another important parameter in the evaluation of a HER electrocatalyst. The long-term durability was tested by repeated potential cycling at a scan rate of 100 mV s⁻¹. As presented in Fig. 5c–e, after 3000 cycles of potential scans, the required overpotential to afford a current density of 10 mA cm⁻² increased by about 35 mV and 43 mV for Pd nanocubes/C and Pt/C, respectively, while barely no change was observed for Pd nanocubes@Mo/C. This indicates that Pd nanocubes@Mo/C possessed remarkably higher durability, probably due to protection of the Mo atoms covered on the surface.

Conclusions

In summary, a facile approach has been developed for the preparation of Pd nanocubes@Mo core-shell nanostructures as high-performance bifunctional catalysts for both ORR and HER. Such core-shell structures were confirmed by TEM and elemental mapping measurements, and further characterized by XRD and XPS analysis. The as-prepared Pd nanocubes@Mo/C exhibited superior ORR performance than Pt/C, evidenced by the more positive onset potential, larger diffusion-limited current, markedly higher specific and mass activities, as well as remarkably higher long-term durability. It also demonstrated apparent HER activity comparable to that of Pt/C along with markedly higher stability. The findings can shed light on design and fabrication of Pd-based core-shell structure as efficient, cost-effective and durable electrocatalysts with dual even multiple functionalities and beyond.

Acknowledgements

Z. H. T. thanks financial support from the National Natural Science Foundation of China (21501059), Science and Technology Program of Guangdong Province (No. 2017A050506014), Guangdong Innovative and Entrepreneurial Research Team Program (No. 2014ZT05N200), as well as Guangdong Natural Science Funds for Distinguished Young Scholars (No. 2015A030306006). S. W. C. acknowledges the National Natural Science Foundation of China for partial support of the work (21528301).

Appendix A. Supplementary data

Supplementary data related to this article can be found at <https://doi.org/10.1016/j.ijhydene.2018.07.097>.

REFERENCES

- [1] Debe MK. Electrocatalyst approaches and challenges for automotive fuel cells. *Nature* 2012;486:43–51.
- [2] Li Y, Dai H. Recent advances in zinc-air batteries. *Chem Soc Rev* 2014;43:5257–75.
- [3] Li Y, Lu J. Metal-air batteries: will they be the future electrochemical energy storage device of choice? *ACS Energy Lett* 2017;2:1370–7.
- [4] Wong WY, Daud WRW, Mohamad AB, Kadhum AAH, Loh KS, Majlan EH. Recent progress in nitrogen-doped carbon and its composites as electrocatalysts for fuel cell applications. *Int J Hydrogen Energy* 2013;38:9370–86.
- [5] Wang W, Lei B, Guo S. Engineering multimetallic nanocrystals for highly efficient oxygen reduction catalysts. *Adv Energy Mater* 2016;6:1600236.
- [6] Wang W, Lv F, Lei B, Wan S, Luo M, Guo S. Tuning nanowires and nanotubes for efficient fuel-cell electrocatalysis. *Adv Mater* 2016;28:10117–41.
- [7] Wang J, Zhang H, Wang X. Recent methods for the synthesis of noble-metal-free hydrogen-evolution electrocatalysts: from nanoscale to sub-nanoscale. *Small Methods* 2017;1700118.
- [8] He G, Song Y, Liu K, Walter A, Chen S, Chen S. Oxygen reduction catalyzed by platinum nanoparticles supported on graphene quantum dots. *ACS Catal* 2013;3:831–8.
- [9] Wang L, Tang Z, Yan W, Wang Q, Yang H, Chen S. Co@Pt Core@Shell nanoparticles encapsulated in porous carbon derived from zeolitic imidazolate framework 67 for oxygen electroreduction in alkaline media. *J Power Sources* 2017;343:458–66.
- [10] Jiang L-Y, Lin X-X, Wang A-J, Yuan J, Feng J-J, Li X-S. Facile solvothermal synthesis of monodisperse Pt₂.6Co₁ nanoflowers with enhanced electrocatalytic activity towards oxygen reduction and hydrogen evolution reactions. *Electrochim Acta* 2017;225:525–32.
- [11] Kuang M, Wang Q, Han P, Zheng G. Cu, Co-Embedded N-Enriched mesoporous carbon for efficient oxygen reduction and hydrogen evolution reactions. *Adv Energy Mater* 2017;7:1700193.
- [12] Wang R, Dong X-Y, Du J, Zhao J-Y, Zang S-Q. Mof-Derived bifunctional Cu₃P nanoparticles coated by a N,P-Codoped carbon shell for hydrogen evolution and oxygen reduction. *Adv Mater* 2017;1703711.

- [13] Liu M, Zhang R, Chen W. Graphene-supported nanoelectrocatalysts for fuel cells: synthesis, properties, and applications. *Chem Rev* 2014;114:5117–60.
- [14] Zhang H, Osgood H, Xie X, Shao Y, Wu G. Engineering nanostructures of PGM-free oxygen-reduction catalysts using metal-organic frameworks. *Nano Energy* 2017;31:331–50.
- [15] Wang M, Chen L, Sun L. Recent progress in electrochemical hydrogen production with earth-abundant metal complexes as catalysts. *Energy Environ Sci* 2012;5:6763–78.
- [16] Erikson H, Sarapu A, Solla-Gullón J, Tammeveski K. Recent progress in oxygen reduction electrocatalysis on Pd-based catalysts. *J Electroanal Chem* 2016;780:327–36.
- [17] Zhang L, Chang Q, Chen H, Shao M. Recent advances in palladium-based electrocatalysts for fuel cell reactions and hydrogen evolution reaction. *Nano Energy* 2016;29:198–219.
- [18] Lu Y, Jiang Y, Gao X, Wang X, Chen W. Strongly coupled Pd nanotetrahedron/tungsten oxide nanosheet hybrids with enhanced catalytic activity and stability as oxygen reduction electrocatalysts. *J Am Chem Soc* 2014;136:11687–97.
- [19] Chen A, Ostrom C. Palladium-based nanomaterials: synthesis and electrochemical applications. *Chem Rev* 2015;115:11999–2044.
- [20] Huang B, Chen L, Wang Y, Ouyang L, Ye J. Paragenesis of palladium–cobalt nanoparticle in nitrogen-rich carbon nanotubes as a bifunctional electrocatalyst for hydrogen-evolution reaction and oxygen-reduction reaction. *Chem Eur J* 2017;23:7710–8.
- [21] Liu S, Mu X, Duan H, Chen C, Zhang H. Pd nanoparticle assemblies as efficient catalysts for the hydrogen evolution and oxygen reduction reactions. *Eur J Inorg Chem* 2017;2017:535–9.
- [22] Deming CP, Mercado R, Gadiraju V, Sweeney SW, Khan M, Chen S. Graphene quantum dots-supported palladium nanoparticles for efficient electrocatalytic reduction of oxygen in alkaline media. *ACS Sustainable Chem Eng* 2015;3:3315–23.
- [23] Deming CP, Mercado R, Lu JE, Gadiraju V, Khan M, Chen S. Oxygen electroreduction catalyzed by palladium nanoparticles supported on nitrogen-doped graphene quantum dots: impacts of nitrogen dopants. *ACS Sustainable Chem Eng* 2016;4:6580–9.
- [24] Chen D, Li C, Liu H, Ye F, Yang J. Core-shell Au@Pd nanoparticles with enhanced catalytic activity for oxygen reduction reaction via core-shell Au@Ag/Pd constructions. *Sci Rep* 2015;5:11949.
- [25] Yuan K, Zhuang X, Fu H, Brunklaus G, Forster M, Chen Y, et al. Two-dimensional core-shelled porous hybrids as highly efficient catalysts for the oxygen reduction reaction. *Angew Chem Int Ed* 2016;55:6858–63.
- [26] Yang H, Tang Z, Yan W, Wang L, Wang Q, Zhang Y, et al. Peptide capped Pd nanoparticles for oxygen electroreduction: strong surface effects. *J Alloys Compd* 2017;702:146–52.
- [27] Yang H, Wen C, Tang Z, Wang L, Wang Q, Yan W, et al. Shape and structural effects of R5-templated Pd nanomaterials as potent catalyst for oxygen electroreduction in alkaline media. *J Mater Sci* 2017;52:8016–26.
- [28] Shao M, Odell J, Humbert M, Yu T, Xia Y. Electrocatalysis on shape-controlled palladium nanocrystals: oxygen reduction reaction and formic acid oxidation. *J Phys Chem C* 2013;117:4172–80.
- [29] Wu J, Shan S, Luo J, Joseph P, Petkov V, Zhong C-J. PdCu nanoalloy electrocatalysts in oxygen reduction reaction: role of composition and phase state in catalytic synergy. *ACS Appl Mater Interfaces* 2015;7:25906–13.
- [30] Lee E, Kwon Y-U. Epitaxial growth of Pd nanoparticles on molybdenum disulfide by sonochemistry and its effects on electrocatalysis. *RSC Adv* 2016;6:47468–73.
- [31] Yan Y, Xia BY, Xu ZC, Wang X. Recent development of molybdenum sulfides as advanced electrocatalysts for hydrogen evolution reaction. *ACS Catal* 2014;4:1693–705.
- [32] Luo Z, Miao R, Huan TD, Mosa IM, Poyraz AS, Zhong W, et al. Mesoporous MoO₃-x material as an efficient electrocatalyst for hydrogen evolution reactions. *Adv Energy Mater* 2016;6:1600528.
- [33] Ma F-X, Wu HB, Xia BY, Xu C-Y, Lou XW. Hierarchical β-Mo₂C nanotubes organized by ultrathin nanosheets as a highly efficient electrocatalyst for hydrogen production. *Angew Chem Int Ed* 2015;54:15395–9.
- [34] Zhang J, Wang T, Liu P, Liao ZQ, Liu SH, Zhuang XD, et al. Efficient hydrogen production on MoNi₄ electrocatalysts with fast water dissociation kinetics. *Nat Commun* 2017;8:15437.
- [35] Xie S, Choi S-I, Lu N, Roling LT, Herron JA, Zhang L, et al. Atomic layer-by-layer deposition of Pt on Pd nanocubes for catalysts with enhanced activity and durability toward oxygen reduction. *Nano Lett* 2014;14:3570–6.
- [36] Wang R, Jiang LY, Feng JJ, Liu WD, Yuan JH, Wang AJ. One-pot solvothermal synthesis of PdCu nanocrystals with enhanced electrocatalytic activity toward glycerol oxidation and hydrogen evolution. *Int J Hydrogen Energy* 2017;42:6695–704.
- [37] Zhang YT, Huang QW, Chang G, Zhang ZL, Xia TT, Shu HH, et al. Controllable synthesis of palladium nanocubes/reduced graphene oxide composites and their enhanced electrocatalytic performance. *J Power Sources* 2015;280:422–9.
- [38] Zhao R, Liu Z, Gong M, Zhang Q, Shi X, Hu Y, et al. Ethylenediamine tetramethylene phosphonic acid assisted synthesis of palladium nanocubes and their electrocatalysis of formic acid oxidation. *J Solid State Electrochem* 2017;21:1297–303.
- [39] Behmenyar G, Akin AN. Investigation of carbon supported Pd–Cu nanoparticles as anode catalysts for direct borohydride fuel cell. *J Power Sources* 2014;249:239–46.
- [40] Fathirad F, Mostafavi A, Afzali D. Bimetallic Pd–Mo nanoalloys supported on Vulcan XC-72R carbon as anode catalysts for direct alcohol fuel cell. *Int J Hydrogen Energy* 2017;42:3215–21.
- [41] Yan W, Tang Z, Li L, Wang L, Yang H, Wang Q, et al. Ultrasmall palladium nanoclusters encapsulated in porous carbon nanosheets for oxygen electroreduction in alkaline media. *ChemElectroChem* 2017;4:1349–55.
- [42] Li D, Tang Z, Chen S, Tian Y, Wang X. Peptide-FlgA3-Based gold palladium bimetallic nanoparticles that catalyze the oxygen reduction reaction in alkaline solution. *ChemCatChem* 2017;9:2980–7.
- [43] Li J-S, Wang Y, Liu C-H, Li S-L, Wang Y-G, Dong L-Z, et al. Coupled molybdenum carbide and reduced graphene oxide electrocatalysts for efficient hydrogen evolution. *Nat Commun* 2016;7:11204.
- [44] Liu Z, Hu JE, Wang Q, Gaskell K, Frenkel AI, Jackson GS, et al. PtMo alloy and MoO_x@Pt core-shell nanoparticles as highly co-tolerant electrocatalysts. *J Am Chem Soc* 2009;131:6924–5.
- [45] Wang L, Tang Z, Yan W, Yang H, Wang Q, Chen S. Porous carbon-supported gold nanoparticles for oxygen reduction reaction: effects of nanoparticle size. *ACS Appl Mater Interfaces* 2016;8:20635–41.
- [46] Shao M, Chang Q, Dodelet J-P, Chenitz R. Recent advances in electrocatalysts for oxygen reduction reaction. *Chem Rev* 2016;116:3594–657.
- [47] Yan W, Tang Z, Wang L, Wang Q, Yang H, Chen S. PdAu alloyed clusters supported by carbon nanosheets as efficient

- electrocatalysts for oxygen reduction. *Int J Hydrogen Energy* 2017;42:218–27.
- [48] Strasser P, Koh S, Anniyev T, Greeley J, More K, Yu C, et al. Lattice-strain control of the activity in dealloyed core–shell fuel cell catalysts. *Nat Chem* 2010;2:454–60.
- [49] Kuo C-H, Lamontagne LK, Brodsky CN, Chou L-Y, Zhuang J, Sneed BT, et al. The effect of lattice strain on the catalytic properties of Pd nanocrystals. *ChemSusChem* 2013;6:1993–2000.
- [50] Zheng J-N, Li S-S, Ma X, Chen F-Y, Wang A-J, Chen J-R, et al. Green synthesis of core–shell gold–palladium@palladium nanocrystals dispersed on graphene with enhanced catalytic activity toward oxygen reduction and methanol oxidation in alkaline media. *J Power Sources* 2014;262:270–8.
- [51] Yang G, Chen D, Lv P, Kong X, Sun Y, Wang Z, et al. Core-shell Au-Pd nanoparticles as cathode catalysts for microbial fuel cell applications. *Sci Rep* 2016;6:35252.
- [52] Feng Y, Liu H, Yang J. A selective electrocatalyst–based direct methanol fuel cell operated at high concentrations of methanol. *Sci Adv* 2017;3, e1700580.
- [53] Feng J-J, Liu L, Ma X, Yuan J, Wang A-J. Ultrasonication-assisted wet-chemical fabrication of uniform AuPt nanodendrites as efficient electrocatalyst for oxygen reduction and hydrogen evolution reactions. *Int J Hydrogen Energy* 2017;42:2071–80.
- [54] Yang J, Wang X, Li B, Ma L, Shi L, Xiong Y, et al. Novel iron/cobalt-containing polypyrrole hydrogel-derived trifunctional electrocatalyst for self-powered overall water splitting. *Adv Funct Mater* 2017;27:1606497.
- [55] Zhang R, Wang X, Yu S, Wen T, Zhu X, Yang F, et al. Ternary NiCo₂Px nanowires as pH-universal electrocatalysts for highly efficient hydrogen evolution reaction. *Adv Mater* 2017;29:1605502.
- [56] Wang X-D, Xu Y-F, Rao H-S, Xu W-J, Chen H-Y, Zhang W-X, et al. Novel porous molybdenum tungsten phosphide hybrid nanosheets on carbon cloth for efficient hydrogen evolution. *Energy Environ Sci* 2016;9:1468–75.
- [57] Fan X, Liu Y, Peng Z, Zhang Z, Zhou H, Zhang X, et al. Atomic H-Induced Mo₂C hybrid as an active and stable bifunctional electrocatalyst. *ACS Nano* 2017;11:384–94.
- [58] Li T, Tang Z, Wang K, Wu W, Chen S, Wang C. Palladium nanoparticles grown on β-Mo₂C nanotubes as dual functional electrocatalysts for both oxygen reduction reaction and hydrogen evolution reaction. *Int J Hydrogen Energy* 2018;43:4932–41.
- [59] Sarkar A, Murugan AV, Manthiram A. Synthesis and characterization of nanostructured Pd-Mo electrocatalysts for oxygen reduction reaction in fuel cells. *J Phys Chem C* 2008;112:12037–43.
- [60] Ensañi AA, Heydari-Soureshjani E, Rezaei B. Three-dimensional graphene promoted by palladium nanoparticles, an efficient electrocatalyst for energy production and storage. *Int J Hydrogen Energy* 2018;43:9652–62.